Journal of Materials Chemistry A

ROYAL SOCIETY OF CHEMISTRY

PAPER

View Article Online
View Journal | View Issue

Check for updates

Cite this: J. Mater. Chem. A, 2024, 12, 20202

Constructing a highly permeable bioinspired rigid-flexible coupled membrane with a high content of spindle-type MOF: efficient adsorption separation of water-soluble pollutants†

Ruilong Zhang,[ab] Jun Zhao, *[bc] Xiaohua Tian,[a] Jian Ye,[a] Lulu Wang,[a] Ifunanya Rejoice Akaniro,[b] Jianming Pan*[a] and Jiangdong Dai *[a]

In recent years, metal–organic frameworks (MOFs) have emerged as a crucial component in the design and fabrication of advanced adsorption separation membranes. The inherent rigidity of these MOF membranes, however, has limited their potential applications in the field of separation technologies. To address these limitations, MOF hybrid membranes have been developed incorporating flexible guest materials. Nevertheless, the proliferation of guest materials has imposed constraints on the advantages inherent to MOFs, and the interactions between these flexible guest materials and MOFs have impeded the progress of MOF membrane technology. Drawing inspiration from the "brick and mortar" structure characteristic of nacre, this study proposed the creation of a rigid-flexible coupled membrane. This innovative approach utilizes a spindle-type MOF as the rigid framework, graphene oxide (GO) as the flexible interlinking component, and tannic acid (TA) as the cross-linking agent. The synthesized coupled membranes (CoFe-MOF/GO–TA) demonstrated exceptional separation efficacy (>98.10%, 210–296 L m^{-2} h^{-1} bar^{-1}) and exhibited outstanding cycling stability in the removal of water-soluble pollutants. Remarkably, after 16 cycles, the permeance to rhodamine B (RhB) was recorded at 230.11 L m^{-2} h^{-1} bar^{-1}, with a rejection of 97.26%, underscoring the superior cycling stability of the MOF hybrid membrane. At the molecular level, the degradation mechanism of RhB was elucidated through a series of experiments and Gaussian calculations, validating the potential of MOFs in pollutant degradation. This discovery provided substantial support for the use of MOFs in the catalytic purification of membranes. Additionally, the MOF hybrid membranes exhibited comparably excellent separation capabilities for both antibiotics and dyes. The bioinspired rigid-flexible coupled membrane demonstrated a synergistic advantage, significantly enhancing the development of MOF hybrid membranes with superior separation performance and remarkable cycling stability.

Received 28th March 2024
Accepted 28th May 2024

DOI: 10.1039/d4ta02063d

rsc.li/materials-a

1 Introduction

Water resources constitute a fundamental cornerstone for the sustenance and advancement of human societies.[1,2] The advent of rapid industrialization and urbanization in recent times has precipitated an alarming increase in the contamination of finite freshwater reserves.[3,4] This phenomenon is acutely evident in the textile and healthcare industries, where the discharge of effluents containing soluble dyes and pharmaceuticals constitutes a severe ecological menace.[5] The intrusion of pollutants into water bodies not only endangers fauna, flora, and microorganisms but also disrupts ecological equilibrium, increasing the propensity for malignancies in humans.[6] This underscores the public health implications of the current ecological crisis.[7] In response to this burgeoning water resource challenge, membrane separation technology has been identified as an efficacious approach.[8] Its inherent attributes, including lower energy requirements, superior separation efficiency, reusability, and versatility across various applications such as seawater desalination, organic solvent separation, gas purification, and wastewater treatment, position it as a viable solution to this dilemma.[9]

Metal–organic frameworks (MOFs),[10,11] a class of crystalline structures, are characterized by a robust structural matrix

[a]Institute of Green Chemistry and Chemical Technology, Advanced Chemical Engineering Laboratory of Green Materials and Energy of Jiangsu Province, School of Chemistry and Chemical Engineering, Jiangsu University, Zhenjiang, China. E-mail: pjm@ujs.edu.cn; daijd@ujs.edu.cn

[b]Department of Biology, Institute of Bioresource and Agriculture, Hong Kong Baptist University, Kowloon Tong, Hong Kong Special Administrative Region, China. E-mail: zhaojun@hkbu.edu.hk

[c]Institute of Advanced Materials, Hong Kong Baptist University, Kowloon Tong, Hong Kong Special Administrative Region, China

† Electronic supplementary information (ESI) available. See DOI: https://doi.org/10.1039/d4ta02063d

formed through the self-assembly of organic ligands and metal ions or clusters *via* coordination bonds. The unique properties of MOFs, including their diverse topologies, customizable pore architectures, extensive specific surface areas, and notable thermal stability,[12] endow them with unparalleled versatility in a range of applications.[13] Significant advancements have been realized in the development of methodologies for the fabrication of MOF hybrid membranes, particularly in the realms of gas and liquid separation.[14,15] The integration of MOFs into hybrid membranes enhances their flexibility and efficacy by incorporating pliable guest materials, thus ameliorating the inherent brittleness of unalloyed MOF membranes.[16–18] However, despite the promising applications of these membranes, enduring challenges persist. These primarily arise from the excessive requirements for guest materials, which impede the effective utilization of the porous characteristics of MOFs and subsequently obstruct efficient water translocation within the structures. Therefore, it becomes imperative to meticulously adjust the MOF composition, while concurrently minimizing guest material content, to optimize performance.[19]

Graphene oxide (GO)[20] has been recognized for its critical role in the architecture and separation of membrane technologies.[21] However, the tendency of GO to disperse in organic solvents and its inclination to cross-link and coordinate with metal ions[22,23] have overshadowed the synergistic potential of MOF and GO combinations. These factors contribute to challenges in achieving homogeneity within GO membrane matrices. The conventional physical blending approach, employed to intersperse MOFs within GO layers, frequently culminates in irregularities and coordination dilemmas, particularly in vacuum filtration matrices.[24] Researchers have been diligently investigating alternative methodologies to enhance the homogeneity of MOF/GO composite membranes. The *in situ* growth paradigm[25] has demonstrated effectiveness in resolving the dispersion and coordination issues inherent between MOF and GO. However, this method can impart rigidity to GO, potentially impacting the separation efficiency of the resultant membrane. Achieving uniformity within GO membranes, especially when integrating MOF and GO, represents a complex challenge. The traditionally adopted physical blending method, which involves dispersing MOFs amidst GO layers, often leads to inconsistencies and coordination issues, a phenomenon especially pronounced in vacuum filtration matrices.[26] To overcome these obstacles, researchers are investigating adjustable techniques to improve uniformity in the MOF/GO composite membrane structure.[20,27,28] Currently, organic compounds such as polyethyleneimine (PEI), polyvinyl alcohol (PVA), dopamine, and polyaniline (PANI) are being utilized as binders and cross-linking agents. These agents facilitate cohesion between GO and MOFs, thereby enhancing membrane stability and separation efficiency.[26,29,30] For example, Liu *et al.* employed polydopamine (PDA) as both a cross-linking agent and reducing agent for GO to prevent uncontrolled aggregation of the MOF (specifically, HKUST-1) within GO layers.[26] Nevertheless, the application of tannic acid (TA),[31] a biopolyphenol, for the reinforcement and enhancement of GO and MOF integrated membranes remains an unexplored avenue.

This study was influenced by the spindle-shaped morphologies[32] observed in biological organisms, which are known to minimize resistance and augment locomotion velocity.[33] These morphologies were incorporated into metal–organic framework (MOF) hybrid membranes to enhance their homogeneity and separation efficacy, thereby advancing the development of high-performance membranes for water purification and environmental improvement. GO and TA were employed as the flexible bridge and cross-linking agent, respectively, in the creation of a high-performance rigid-flexible coupled membrane (CoFe-MOF/GO–TA), specifically designed for the adsorption separation of water-soluble pollutants. To examine the impact of GO–TA on the surface and cross-sectional morphology of the MOF hybrid membrane, scanning electron microscopy (SEM) imaging was conducted. Additionally, the charge properties and dispersive characteristics of GO and MOF were investigated *via* zeta potential measurement, providing insights into the modulating influence of TA. Furthermore, the degradation efficacy of CoFe-MOF for pollutants was probed utilizing potassium persulfate (PMS) activation, and the typology of free radicals generated within the reaction milieu was elucidated using electron paramagnetic resonance (EPR). The optimization of GO–TA and CoFe-MOF conditions to realize optimal separation efficacy is systematically explored. The results showed that the CoFe-MOF/GO–TA-10 membrane demonstrated exemplary separation performance, cycling robustness, and universal applicability, laying a robust foundation for practical implementation. This study underscored the latent promise of MOF hybrid membranes in the realm of water treatment and environmental revitalization.

2 Materials and methods

2.1 Materials

All chemicals were used in their original state. Refer to the ESI† for further details.

2.2 Preparation of spindle-type CoFe-MOF

The synthesis of spindle-type CoFe-MOF was conducted using the solvothermal method. Initially, 3.714 g of fumaric acid (FA) was dissolved in 40 mL of *N*,*N*-dimethylformamide (DMF). Subsequently, 0.806 g of ferric nitrate nonahydrate ($Fe(NO_3)_2 \cdot 9H_2O$) and 0.290 g of cobalt nitrate hexahydrate ($Co(NO_3)_2 \cdot 6H_2O$) were added and stirred until a homogeneous solution formed. The resultant solution was then transferred to a high-pressure hydrothermal kettle and maintained at 120 °C for 6 h. After cooling to room temperature, the product was collected through centrifugation, washed, and dried, yielding a spindle-shaped MOF denoted as CoFe-MOF. GO powder was prepared utilizing the modified Hummers' method.[34]

2.3 Preparation of the CoFe-MOF/GO–TA composite membrane

A dispersion of CoFe-MOF with a concentration of 50 mg L^{-1} was prepared through ultrasonic dispersion. A specific quantity of GO powder was introduced into 20.0 mg L^{-1} of TA solution.

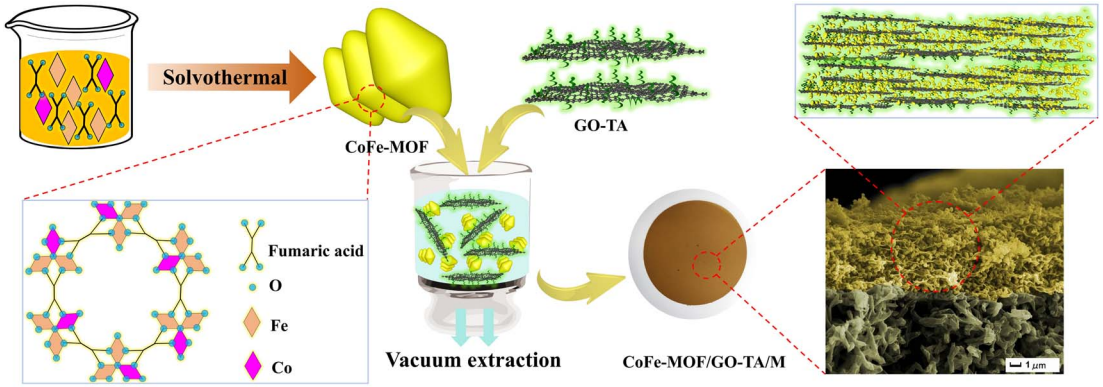

Scheme 1 Schematic diagram of the preparation of the CoFe-MOF/GO–TA membrane.

Following ultrasonication, a GO–TA solution was obtained with the GO concentration denoted as x. Subsequently, 50 mL of the CoFe-MOF dispersion was combined with 50 mL of the GO–TA solution. The resulting mixture underwent filtration through a PVDF membrane using vacuum filtration, resulting in the formation of a composite membrane denoted as CoFe-MOF/GO–TA-x (Scheme 1). And the membrane name and the CoFe-MOF proportion are shown in Table S1.† Notably, the discussion of MOF content excluded the mass of TA due to its lower mass contribution to the membrane composition. For instance, if the concentration of GO used was 10.0 mg L^{-1}, the composite membrane would be labeled as CoFe-MOF/GO–TA-10.

2.4 Characterization

All characterization details, the FTIR analysis (Fig. S4a†) and the stress–strain curves (Fig. S4b†) are provided in the ESI.†

2.5 Filtration of pollutants

To examine the filtration efficiency of the MOF hybrid membrane for water-soluble pollutants, various categories of pollutants were generated at a concentration of 10 mg L^{-1}. The impact of different operational pressures on the separation efficiency of the composite membranes was subsequently investigated. Permeance (L m^{-2} h^{-1} bar^{-1}) and flux (L m^{-2} h^{-1}) were calculated according to eqn (1) and (2), respectively. Rejection (%) was quantified using a UV spectrophotometer, as specified by using eqn (3).

$$\text{Permeance} = \frac{V}{A \times t \times P} \quad (1)$$

$$\text{Flux} = \frac{V}{A \times t} \quad (2)$$

$$\text{Rejection} = \frac{C_0 - C_t}{C_0} \times 100\% \quad (3)$$

Here, the variable A represented the effective filtration area (m^2) of the scrutinized membrane, V (L) denoted the volume of the filtrate solution, and t (h) indicated the filtration duration. P stood for the pressure applied in the filtration process. Furthermore, C_t and C_0 symbolized the concentrations of pollutant solutions after and before membrane filtration, respectively.

2.6 Adsorption of pollutants

To analyze the adsorption kinetics of CoFe-MOF powder on pollutants (such as RhB, PS, and TC), a meticulously prepared 100 mL solution containing RhB (20 mg L^{-1}) was employed, with the introduction of 20 mg of CoFe-MOF powder. The mixed solution was maintained at 25 °C, and specimens were extracted at specified intervals. Subsequently, the samples underwent filtration using a membrane, and the concentration of pollutants in the filtrate was quantified by gauging the UV maximum absorption peak. The real-time adsorption amount of the pollutant by CoFe-MOF (Q_t, mg g^{-1}) was computed employing eqn (4). For determining the equilibrium adsorption capacity of CoFe-MOF on pollutants, 2.0 mg of CoFe-MOF was incorporated into 10 mL of a RhB solution (20 mg L^{-1}) at 25 °C. Following 24 h of adsorption equilibrium, the residual concentration of pollutants was ascertained, and the equilibrium adsorption capacity (Q_e, mg g^{-1}) was calculated using eqn (5).

$$Q_t = \frac{(C_0 - C_t) \times V}{m} \quad (4)$$

$$Q_e = \frac{(C_0 - C_e) \times V}{m} \quad (5)$$

Here, C_t (mg L^{-1}) denoted the remaining pollutant concentration after adsorption for a duration of time t (min), while C_e (mg L^{-1}) indicated the equilibrium concentration of the pollutant. V (L) represented the volume of the solution and m (g) indicated the mass of CoFe-MOF.

2.7 Degradation of pollutants

2.7.1 Static degradation. 3 mg of CoFe-MOF was introduced into a 50 mL pollutant solution (20 mg L^{-1}), followed by the addition of 50 mL of PMS solution (100 mg L^{-1}) at 25 °C. The efficacy of degradation was assessed utilizing a UV spectrophotometer and computed using C_t/C_0. The rate constant (k) related to organic pollutants was determined employing a first-order equation (eqn (6)).

2.7.2 Quenching experiment. Quenchers such as methanol (MA), *tert*-butanol (TBA), *p*-benzoquinone (*p*-BQ), and furfuryl alcohol (FFA) were employed. The concentration ratio of

quenchers to PMS was kept at 200 : 1 to analyze the impact of various free radicals on the degradation of RhB during the process.

$$\ln\frac{C_t}{C_0} = -kt \quad (6)$$

2.8 Catalytic-cleaning cycle process

For instance, during the filtration of a 10 mg L^{-1} pollutant solution, a filtration procedure was executed for 5 min, followed by the introduction of 100 mg L^{-1} PMS into an ultrafiltration cup for a duration of 5 min. Subsequently, the cup underwent a wash with deionized water for 5 min to guarantee thorough removal of PMS. The entire filtration and cleaning procedures constituted a catalytic-cleaning cycle. The separation efficiency of the composite membrane for the pollutant was evaluated after multiple cycles.

2.9 Exploring long-term effectiveness

20 mL of RhB solution (10 mL L^{-1}) was filtered through the same membrane, which was repeated many times for investigating the long-term effectiveness. The rejection rate of each filtration was determined using eqn (3). The separation performance was indicated by C/C_0, representing the cumulative filtered volume. The real-time adsorption capacity of the composite membrane was calculated based on the total filtered volume, as obtained from eqn (4).

2.10 Computational methods

Geometric optimization and the calculation of single-point energy were performed using the Gaussian 09 software[35] at the B3LYP/6-31+G(d,p) level of theory. To assess the distribution of charge and unpaired spin at distinct sites within both the RhB molecule and the radical, electron spin densities were determined *via* natural bond orbital analysis.[36] The explication of regioselectivity for free radical attacks on the RhB molecule was established using Fukui indices.[37] Importantly, the Fukui function played a pivotal role in DFT, a methodology widely employed for anticipating reactive sites susceptible to radical attacks. The Fukui function was precisely defined in eqn (7).

$$\text{Nucleophilic attack}: \ f(r) = \left[\frac{\partial_{\rho(r)}}{\partial_N}\right]_V \quad (7)$$

Here, $\rho(r)$ denoted the electron density at a spatial point r, with N representing the electron count in the current system. The constant term v in the partial derivative pertained to the external potential. The Fukui function for a particular molecular system was computed by employing the electron density of three states, as illustrated in eqn (8).[38]

$$\text{Radical attack}: \ f_k^0 = \left(q_{N-1}{}^k - q_{N+1}{}^k\right)/2 \quad (8)$$

Here, in the aforementioned equation, N denoted the quantity of electrons in the existing molecular system. Both the $N-1$ and $N+1$ states exhibit identical molecular geometries to the N state. The reactivity descriptor for a radical attack was denoted by f_k^0. Atoms characterized by larger Fukui functions corresponded to heightened reactivity levels.

3 Results and discussion

3.1 Morphologies and chemical composition

The morphology of CoFe-MOF was scrutinized using SEM and TEM. As shown in Fig. 1a and b, the CoFe-MOF particles displayed a consistent size distribution. The pseudo-color SEM image (Fig. 1a) illustrated a spindle-type morphology resembling a spindle (as shown in the illustration of Fig. 1a), with a length of approximately 450 nm and a diameter of around 270 nm. EDS-mapping images (Fig. S1†) identified distinct elemental signatures for C, O, Fe, and Co elements, with atomic contents of 39.99%, 52.01%, 5.11%, and 2.89%, respectively. The atomic content ratio of Fe to Co was approximately 2 : 1, mirroring the initial raw material ratio and confirming the successful incorporation of Co into the MOF structure. TEM images (Fig. 1b and c) portrayed uniformly sized CoFe-MOF particles without agglomeration, indicating favorable dispersibility. Moreover, high-magnification TEM images revealed a rough surface texture on the CoFe-MOF particles. This surface characteristic is hypothesized to provide an extended pathway for the penetration of water molecules in the composite membrane, potentially enhancing its filtration efficiency.

Fig. 1d and S2a† depict the surface of CoFe-MOF/GO–TA-0, which was characterized by the presence of numerous cracks and an accumulation of CoFe-MOF nanoparticles. In the cross-sectional view of CoFe-MOF/GO–TA-0 (Fig. S3a†), it was observed that CoFe-MOF/GO–TA-0 was deposited on the surface of the base membrane. With an increase in the GO–TA concentration, the presence of surface cracks diminished, and an increasing amount of the GO–TA layer was observed connecting the CoFe-MOF particles (Fig. 1e and S2b–2f†). At a concentration of 20 mg L^{-1} (Fig. S2f†), the surface exhibited minimal porosity, while high-magnification images revealed the copious presence of GO layer wrapping within the pores. In the SEM images of the composite membrane cross-section (Fig.S3a–f†), the increase in GO–TA concentration improved the hierarchical phenomenon, where numerous spindle-type CoFe-MOF particles were dispersed between GO–TA sheets, exhibiting a bioinspired rigid-flexible coupled membrane. Obviously, with a decrease in the CoFe-MOF proportion, the GO–TA layer appeared clearer and denser. Here GO and TA served as a 2D flexible bridge and the green biomolecule cross-linking agent, respectively. Under the premise of a well-defined hierarchical organization, the GO–TA mesh-like structure was conducive to the removal of contaminants in water. It is noteworthy that 83.33% of CoFe-MOF was present in the MOF hybrid membrane for the CoFe-MOF/GO–TA-10 cross-section (Fig. 1f). The cross-sections of CoFe-MOF/GO–TA-10 underwent EDS-mapping analysis (Fig. S3g†), revealing a uniform distribution of C, O, Fe, and Co elements on the composite membrane, devoid of noticeable element aggregation. On the other hand, in the interfacial region between the base membrane and CoFe-MOF/GO–TA section, the absence of any discernible cracks elucidated the exceptional characteristics of the composite membrane.

X-ray diffraction (XRD) was employed to analyze the crystal structures of CoFe-MOF and CoFe-MOF/GO–TA. The XRD

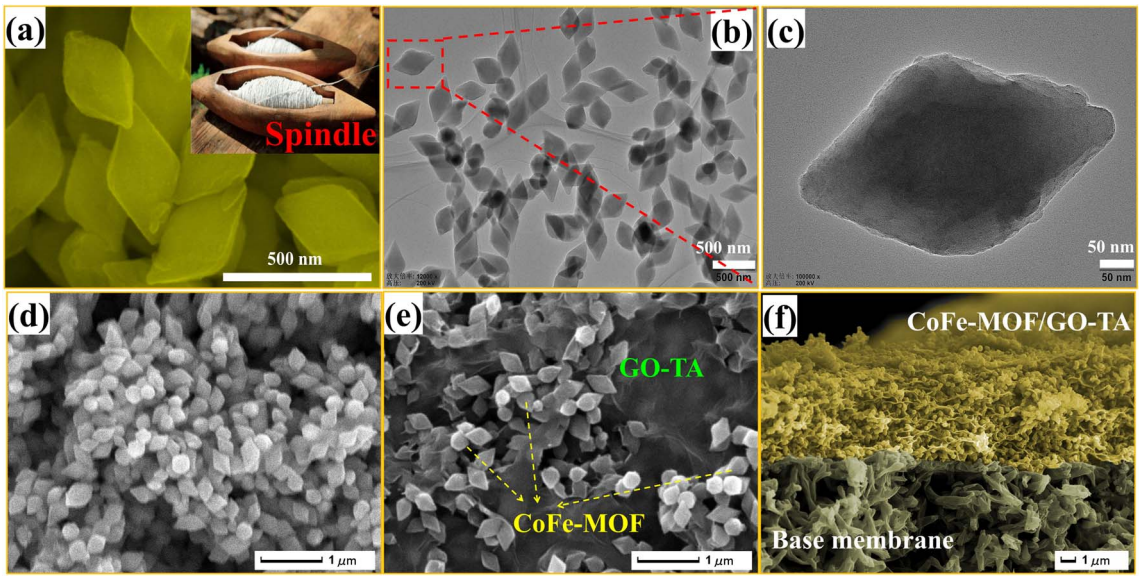

Fig. 1 SEM image of CoFe-MOF (a), TEM images of CoFe-MOF (b and c), and SEM images of the CoFe-MOF/GO–TA-0 surface (d), CoFe-MOF/GO–TA-10 surface (e) and CoFe-MOF/GO–TA-10 cross-section (f).

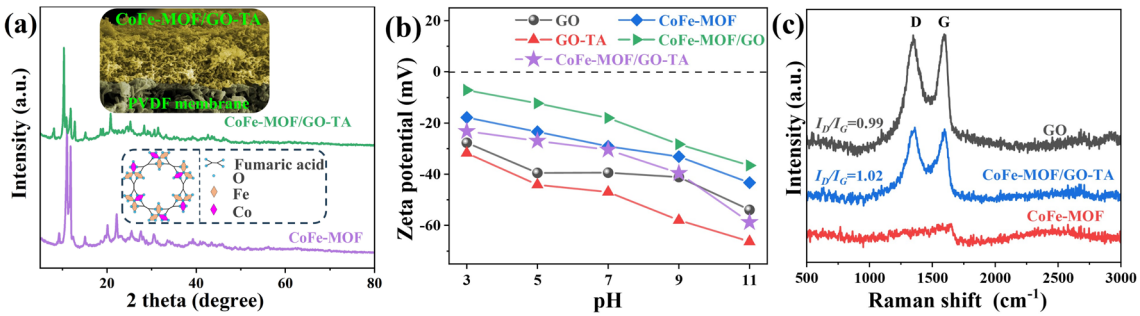

Fig. 2 XRD pattern (a), zeta potential measurement (b) and Raman spectra (c).

diffraction pattern of CoFe-MOF (Fig. 2a) exhibits peaks similar to those of Fe-MIL-88A,[39] affirming the successful formation of CoFe-MOF. The shift in 2θ resulted from the substitution of Fe^{3+} by Co^{2+} in the trimer cluster of Fe-MIL-88A,[40] leading to coordination defects in CoFe-MOF. The XRD pattern of CoFe-MOF/GO–TA displayed slight changes in peak position and intensity, indicating the *in situ* assembly of GO–TA with Fe^{3+} and Co^{2+} in CoFe-MOF, although no significant alterations in the crystal structure were observed. Zeta potential analysis of surface charge was utilized to assess the interaction between CoFe-MOF and GO–TA, as well as the stability of the mixed solution (Fig. 2b). The addition of TA enhanced the stability of GO, as the zeta potential of GO–TA was lower than that of GO but remained highly negative. CoFe-MOF demonstrated good dispersion ability under neutral conditions, with a zeta potential of −29.07 mV at pH = 7. The mixed solution of GO and CoFe-MOF exhibited poor stability at pH = 7, with a zeta potential of −17.97 mV. Nevertheless, the zeta potential of CoFe-MOF/GO–TA gradually decreased with increasing pH, reaching −30.42 mV at pH = 7, indicating the commendable stability of the mixed solution. TA played a pivotal role in the preparation of CoFe-MOF/GO–TA by preventing coordination between GO and metal cations in CoFe-MOF, enhancing the stability of the mixed solution, and resulting in a more uniform morphology of the composite membrane. In the Raman spectra (Fig. 2c), CoFe-MOF did not exhibit any noticeable D and G peaks due to the absence of GO. The I_D/I_G value of 0.99 for the GO powder indicated a substantial number of defects. The I_D/I_G value of CoFe-MOF/GO–TA increased significantly (I_D/I_G = 1.02), indicating a reduction in the order degree of GO sheets during the membrane formation process of GO–TA solution and CoFe-MOF dispersion by vacuum filtration. As shown in Fig. S5,† the SBET values of CoFe-MOF and CoFe-MOF/GO–TA (powder) were 8.03 and 6.81 $m^2\ g^{-1}$, respectively. This indicated that the specific surface area of CoFe-MOF decreased after the addition of GO–TA, along with a reduction in pore volume (V_m). This reduction could be attributed to the filling of TA and GO in the surface defects of CoFe-MOF. Additionally, the average pore size (Daver) significantly increased, which was attributed to the formation of a gap between GO and the MOF (Table S2†). This

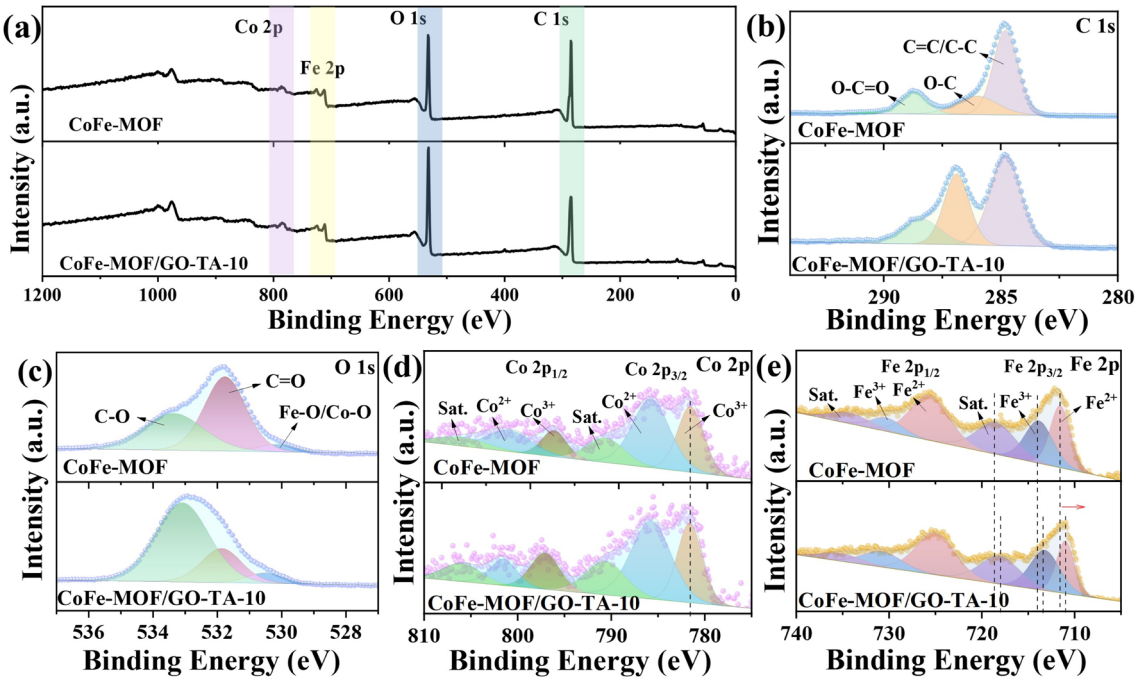

Fig. 3 XPS survey spectra (a), C 1s (b), O 1s (c), Co 2p (d), and Fe 2p (e) XPS spectra of CoFe-MOF and CoFe-MOF/GO–TA-10.

Table 1 Element content of CoFe-MOF and CoFe-MOF/GO–TA-10

Sample/element	C 1s (%)	O 1s (%)	Co 2p (%)	Fe 2p (%)
CoFe-MOF	73.94	22.08	1.35	2.63
CoFe-MOF/GO–TA-10	67.13	29.63	1.06	2.18

decrease resulted from the intercalation of CoFe-MOF particles into the GO layer.

To further scrutinize the chemical composition of CoFe-MOF and CoFe-MOF/GO–TA-10 surfaces, XPS analysis was conducted. As shown in Fig. 3a, the XPS survey spectra of CoFe-MOF revealed four signals of C 1s, O 1s, Co 2p, and Fe 2p, with contents of 73.94%, 22.08%, 1.35%, and 2.63%, respectively. Notably, the Co and Fe element content closely approximated a 1 : 2 ratio, indicating the successful doping of the Co element during the preparation of CoFe-MOF (Table 1). The XPS survey spectra of CoFe-MOF/GO–TA-10 included four elements: C, O, Co, and Fe, with contents of 67.13%, 29.63%, 1.06%, and 2.18%, respectively. The increased content of the O element can be attributed to the presence of GO and TA. As shown in Fig. 3b, C 1s XPS spectra of CoFe-MOF predominantly comprised C–C/C=C, C–O, and C–O=C at 284.8, 286.0, and 288.7 eV, primarily due to the carbon element of FA. Similar peaks were observed for C 1s XPS spectra of CoFe-MOF/GO–TA, with an increased C–O content due to the presence of GO and TA molecules. Fig. 3c demonstrates a significant increase in C–O content, indicating a substantial amount of GO–TA on the surface of the composite membrane, which was consistent with the SEM image of CoFe-MOF/GO–TA-10 (Fig. 1e and f). In Co 2p XPS spectra (Fig. 3d), three peak types of Co^{3+}, Co^{2+}, and Sat. were observed for both CoFe-MOF and CoFe-MOF/GO–TA, with comparable peak positions. However, the content of Co^{2+} slightly increased in CoFe-MOF/GO–TA, implying that TA exerted a certain reduction effect on Co^{3+}. Notably, there was a significant shift in Fe XPS spectra of CoFe-MOF/GO–TA-10 towards low binding energy, which indicated that TA possessed good reducibility for transition metals (Fig. 3e). And specific data are presented in Table 2.

Table 2 Analysis data of C 1s, O 1s, Co 2p, and Fe 2p XPS spectra for CoFe-MOF and CoFe-MOF/GO–TA-10

Element (%)/sample		CoFe-MOF	CoFe-MOF/GO–TA-10
C 1s	C=C/C–C	60.47	50.03
	C–O	22.49	32.69
	C–C=O	17.04	17.28
O 1s	Fe–O/Co–O	4.74	6.10
	C=O	55.75	23.02
	C–O	39.51	70.88
Co 2p	Co^{3+}	32.65	34.16
	Co^{2+}	48.51	41.97
	Sat.	18.84	22.87
Fe 2p	Fe^{3+}	25.71	31.17
	Fe^{2+}	47.56	44.33
	Sat.	26.73	24.51

3.2 Membrane separation performance

The separation efficiency of CoFe-MOF/GO–TA depended on the concentration of the GO–TA solution, maintaining a GO and TA concentration ratio of 1 : 2. For clarity, the concentration of the GO–TA solution was denoted by using the concentration of GO. The optimal concentration of the GO–TA solution was determined through experiments using RhB and TC as model pollutants. As

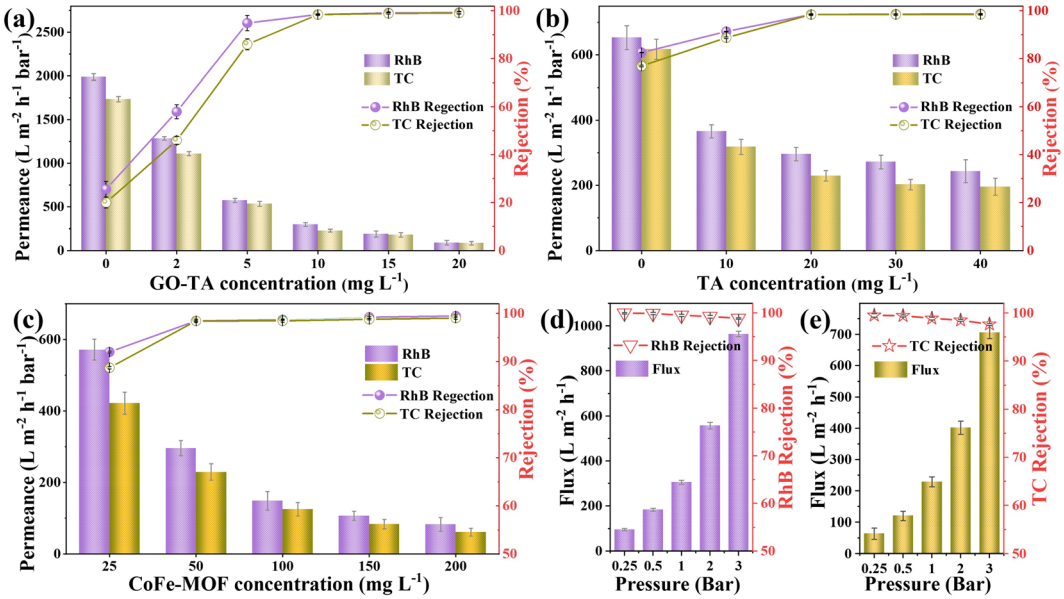

Fig. 4 Effects of GO–TA concentration (a), TA concentrations (b), CoFe-MOF concentration (c), and operating pressure (d and e) on separation performance.

depicted in Fig. 4a, the permeance of RhB and TC solutions decreased significantly, while rejection increased with the increase in GO–TA concentration. At a concentration of 10.0 mg L^{-1}, the permeance of RhB and TC was 296.17 and 229.29 L m^{-2} h^{-1} bar^{-1}, respectively, with rejections reaching 98.45% and 98.43%, respectively. Nevertheless, further increments in GO–TA concentration led to a sharp decline in the permeance, with no substantial change in the pollutant rejection. Consequently, 10.0 mg L^{-1} was identified as the optimal concentration of the GO–TA solution. As shown in Fig. 4b, CoFe-MOF/GO–TA prepared with GO–TA showed better rejection than CoFe-MOF/GO (TA concentration was 0 mg mL^{-1}). At a concentration of 20.0 mg L^{-1}, the rejections of RhB and TC were 98.45% and 98.43%, respectively. As the concentration of the TA solution continued to increase, the

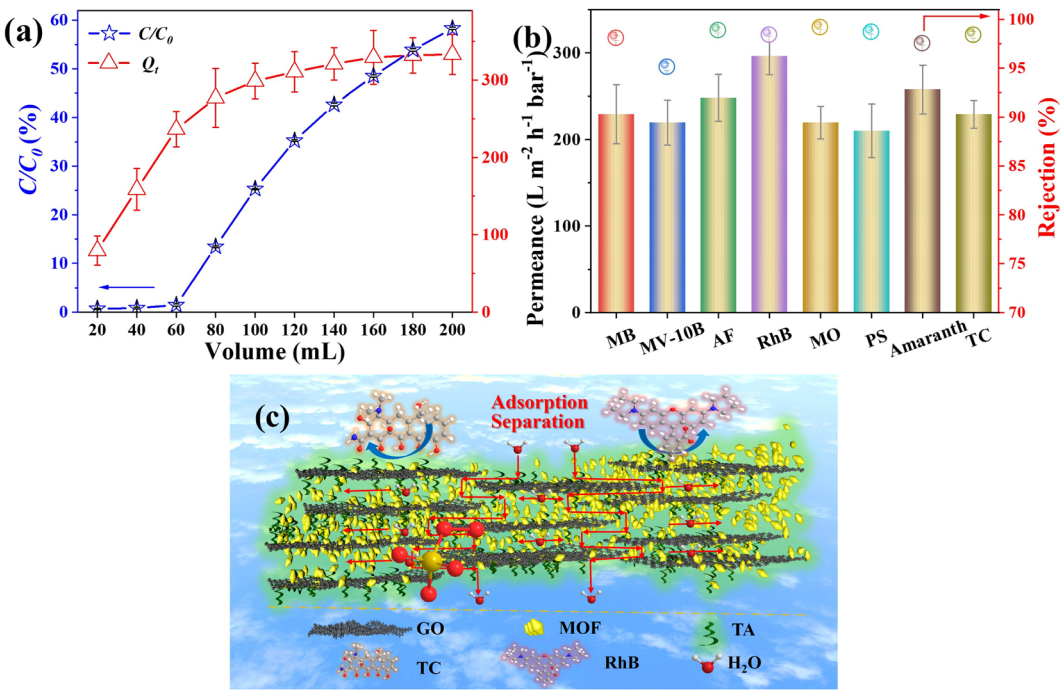

Fig. 5 Dynamic adsorption performance for RhB (a) and separation performance for different pollutants (b), and the membrane separation mechanism (c).

permeance gradually decreased, but the rejection did not significantly increase, and 20.0 mg L^{-1} was considered the optimal concentration of the TA solution. The impact of CoFe-MOF concentration on the separation efficiency of the composite membrane was investigated with a CoFe-MOF and GO–TA concentration ratio of 5 : 1, as shown in Fig. 4c. At a CoFe-MOF concentration of 25 mg L^{-1}, the permeances of CoFe-MOF/GO–TA for RhB and TC were 571.68 and 422.04 L m^{-2} h^{-1} bar^{-1}, respectively, with rejections of only 91.96% and 88.69%. However, at a CoFe-MOF concentration of 50 mg L^{-1}, the rejections of RhB and TC by CoFe-MOF/GO–TA reached 98.45% and 98.43%, respectively. With the increase in CoFe-MOF concentration, the rejection gradually increased, but the permeances decreased rapidly. At a concentration of 50 mg L^{-1}, the permeances of RhB and TC decreased to 82.58 and 61.34 L m^{-2} h^{-1} bar^{-1}. Therefore, a CoFe-MOF concentration of 50 mg L^{-1} could achieve efficient retention of pollutants.

The influence of different operating pressures on pollutant retention is a pivotal aspect to consider when evaluating membrane separation performance. To scrutinize this aspect, CoFe-MOF/GO–TA-10 was selected as a sample. In Fig. 4d, CoFe-MOF/GO–TA-10 demonstrated effective retention of RhB under varying pressures. At 0.25 bar, the flux measured 96.37 L m^{-2} h^{-1}, and the RhB rejection reached 99.94%. The flux gradually increased with escalating pressure, although the RhB rejection experienced a slight decrease, reaching 98.84% at 3.0 bar. This reduction in the rejection at higher pressures may be ascribed to the increased penetration of water molecules, facilitating the permeation of RhB molecules. Similarly, with increasing pressure, the flux increased while the TC rejection exhibited a slight decrease (Fig. 4e). Nevertheless, the rejection remained high, reaching 97.65% at 3.0 bar. These findings indicated that CoFe-MOF/GO–TA-10 could achieve effective pollutant rejection across a wide range of operating pressures (0.25–3.0 bar).

3.3 Catalytic-cleaning performance and mechanism

Fig. 5 shows the separation performance of the MOF hybrid membrane. At a volume of 80 mL, the adsorption amount (Q_e) reached 236.52 mg g^{-1}, C/C_0 witnessed a significant increase, indicating RhB permeation leakage (Fig. 5a). In the long-term separation process for RhB (Fig. S7†), after 200 mL of filtration, the rejection decreased to 1.71%. CoFe-MOF/GO–TA-10 was nearing adsorption saturation, with an adsorption capacity of 331.99 mg g^{-1}, surpassing the adsorption capacity of CoFe-MOF powder by 15.90 times (as shown in Fig. S9a†). Fig. S8† depicts the mass spectrum of RhB before and after filtration using CoFe-MOF/GO–TA-10. Remarkably, the mass spectrometry information remained nearly identical before and after filtration. This indicated that the composite membrane achieved ultra-fast adsorption during the filtration process, likely due to its limited enrichment effect on RhB, rather than degradation. Therefore, the composite membrane could achieve ultra-fast adsorption during the filtration process, attributed to its limited enrichment effect on RhB. To examine the universality of separation for the MOF hybrid membrane, various pollutants underwent separation by CoFe-MOF/GO–TA-10, as depicted in Fig. 5b. The rejections of AF, RhB, MO, PS, and TC were 98.91%, 98.45%, 99.22%, 98.74%, and 98.43%, respectively, with permeances ranging from 210 to 296 L m^{-2} h^{-1} bar^{-1}. The composite membrane also exhibited notable rejections for MB, MV-10B, and amaranth, measuring 98.12%, 95.15%, and 97.57%, respectively, with permeance exceeding 220 L m^{-2} h^{-1} bar^{-1}. The slight discrepancies might arise from differences in the size and charge properties of the pollutant molecules (Fig. S6†). Additionally, when compared with the literature (Table 3), CoFe-MOF/GO–TA-10 demonstrated superior separation advantages and catalytic-cleaning performance.

Table 3 Performance comparison of CoFe-MOF/GO–TA and GO composite membranes in the literature

Membrane	Pollutant	Permeance (L m^{-2} h^{-1} bar^{-1})	Rejection (%)	Catalytic cleaning	Guest material proportion (%)	Ref.
prGO/COF-0.3	MB	194	98	Without	23	44
eZIF-8/GO	CR	28.25–45.4	99	Without	45.5	27
PVDF/TC14-GO/TiO_2	MB	4.9	92.61	Without	—	45
ZIF-8@f-GOm	MB	60	~100	Without	—	20
PAA@UiO/GO	MB, RB, CR	100	95	Without	66.6	46
GO/Cu-TCPP	CR	165.2	99.1	Without	—	28
prGO@cHKUST-1	MB	210.7	99.5	Without	—	12
GO/M88A	MB	28.7	99.58	Photo-Fenton	—	24
G-2 membrane	MLB, MB, EB	130.0	>89.6%	Photo-Fenton	—	47
PAA@NM88B/GO	MB, CR, CV	68.21	>97%	Photo-Fenton	66.6	48
GO/PB membrane	MB, RhB, CR	>139.3	>97.5%	Photo-Fenton	63.3	49
TFC-GB-0.11 membrane	OFLX, RhB, basic blue 26	26.6	~100%	Photocatalytic	—	50
GO/PAA/CATC membrane	MB, RhB, CR	30.95	>99%	Photocatalytic	92.3	51
CuTz-1/GO	CR	40.2	99.4	Photocatalytic	62.3	29
FeCo@GCTs/GO	MB	487.3	52.4	PMS	96.1	21
NiCo-LDH-GTP/GO-5 and NiCo-LDH-BTP/GO-5	RhB, MB	85.98 and 90.76	98.73% and 99.54%	PMS	90.9	9
CoFe-MOF/GO–TA-10	RhB	296.17	98.45	PMS	83.3	This work
CoFe-MOF/GO–TA-10	TC	229.29	98.43	PMS	83.3	

Although the surface of CoFe-MOF/GO–TA exhibited negative charges (Fig. 2b), it demonstrated outstanding separation performance not only for positively charged pollutants (*e.g.* MB, RhB, and MV-10B) but also for negatively charged (*e.g.* PS, AF, amaranth, and MO) and neutral pollutants (*e.g.* TC). This phenomenon may have arisen from the facile interaction between functional groups on the pollutant molecules and those on the membrane, encompassing π–π interactions, coordination effects, electrostatic attraction, and hydrogen bonding.[41,42] Particularly significant were the roles played by the benzene rings, –OH, and –COOH on the surfaces of GO and TA. It is worth noting that the composite membrane adopted a porous structure, with pore sizes significantly exceeding the dimensions of the pollutant molecules.[43] Therefore, it is reasonable to infer that pollutant removal was primarily driven by adsorption mechanisms (Fig. 5c).

The investigation scrutinized the adsorption performance of CoFe-MOF on TC, PS, and RhB. The findings revealed saturated adsorption capacities of CoFe-MOF for the three pollutants to be 26.21, 30.71, and 20.88 mg g^{-1}, respectively (Fig. S9a†). Within the initial 60 min, a rapid adsorption rate was observed (Fig. S9b†), followed by a subsequent deceleration, possibly attributed to the saturation of adsorption sites. The fitting curve for quasi-second-order kinetics (Fig. S9d†) exhibited a higher correlation coefficient compared to the quasi-first-order kinetics curve (Fig. S9c†), suggesting that the primary adsorption mechanism was chemical in nature. The investigation further identified that CoFe-MOF not only facilitated the effective degradation of pollutants but also enhanced the separation capabilities of the MOF hybrid membranes. The degradation efficacy of CoFe-MOF was explored using RhB as an illustrative case. The results revealed that during the degradation of RhB by CoFe-MOF (Fig. 6a), complete RhB degradation was achieved in 16 min, highlighting its remarkable degradation performance. The 3D fluorescence spectrogram depicting the degradation process of RhB (Fig. S10†) demonstrated that after 20 min of degradation, the fluorescence within the 500–700 nm excitation wavelength range had nearly vanished, signifying the thorough degradation of RhB. A similar phenomenon was observed for the degradation of TC, which was represented by antibiotics (Fig. S11†). In summary, the findings indicated that CoFe-MOF exhibited outstanding pollutant degradation capabilities in water within a PMS system.

To investigate the involvement of reactive oxygen species in pollutant degradation in the CoFe-MOF/PMS system, a quenching experiment was executed using RhB degradation by using CoFe-MOF as a representative case. Methanol (MA), *tert*-butanol (TBA), furfuryl alcohol (FFA), and *p*-benzoquinone (*p*-BQ) were selected as quenchers.[21,52] The impact of $^{\bullet}OH$ and $SO_4^{\bullet-}$ on the degradation process was assessed using MA as the quenching agent. As shown in Fig. 6b, C_t/C_0 was 47.07% after 20 min in the presence of MA, signifying that MA substantially mitigated the influence of CoFe-MOF on RhB, indicating a substantial contribution of $^{\bullet}OH$ and $SO_4^{\bullet-}$ to the degradation process. Additionally, TBA was employed to quench $^{\bullet}OH$. With TBA present, the C_t/C_0 of RhB was 10.63% after 20 min of degradation, suggesting a discernible role of $^{\bullet}OH$ in the degradation process. FFA demonstrated effective quenching of $^1O_2$, with a C_t/C_0 of 17.16% after 20 min, underscoring the significant involvement of $^1O_2$ in the degradation process. p-BQ exhibited remarkable quenching of $O_2^{\bullet-}$ during the reaction, and the C_t/C_0 of RhB was 14.94% after 20 min, indicating the crucial role of $O_2^{\bullet-}$ in the degradation process. The generation of $^{\bullet}OH$, $SO_4^{\bullet-}$, $O_2^{\bullet-}$, and $^1O_2$ in the CoFe-MOF/PMS system was

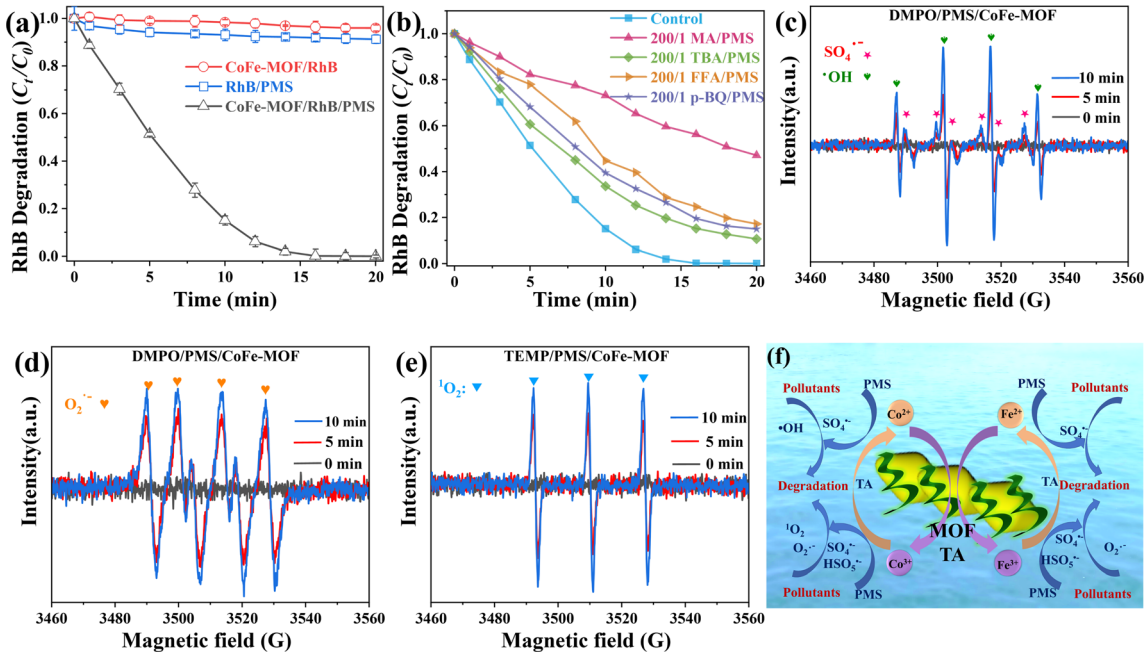

Fig. 6 Degradation process (a) and radical quenchers (b) in the CoFe-MOF/PMS/RhB system, EPR spectra of DMPO-$HO^{\bullet}$ and DMPO-$SO_4^{\bullet-}$ (c), DMPO-$O_2^{\bullet-}$ (d) and TEMP-$^1O_2$ (e) and the degradation mechanism (f) in the CoFe-MOF/PMS system. Conditions: [catalyst] = 20 mg L^{-1}, [RhB] = 20 mg L^{-1}, [PMS] = 100 mg L^{-1}.

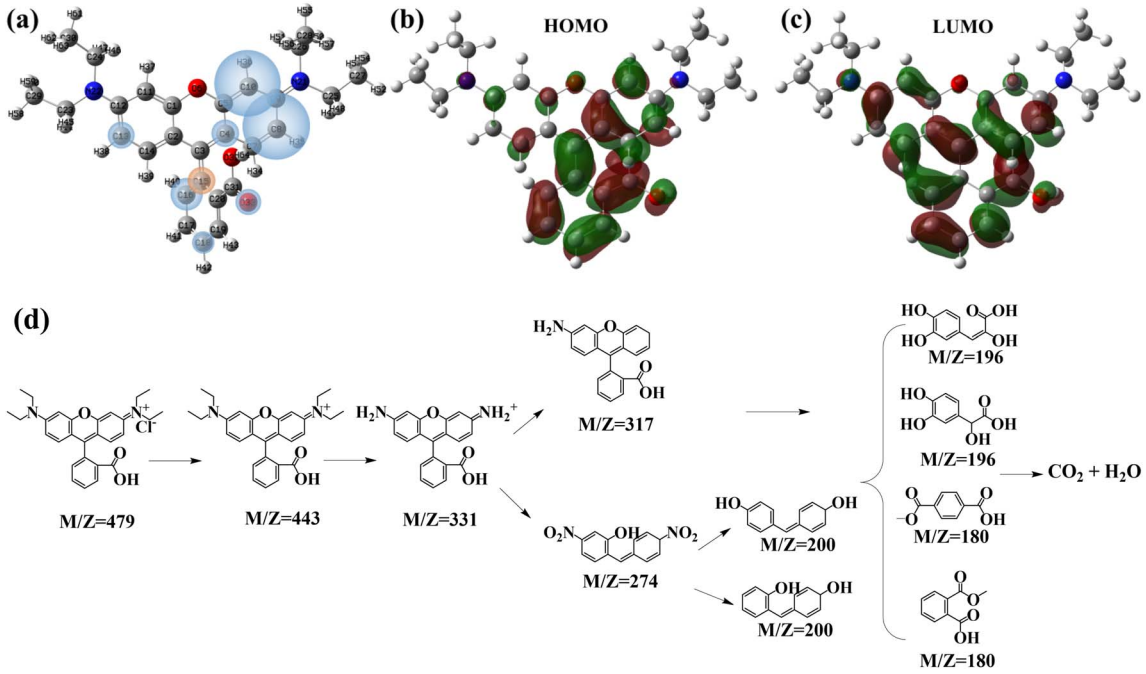

Fig. 7 Molecular structure (a), frontier molecular orbitals HOMO (b) and LUMO (c) and the potential degradation pathway of RhB (d).

evidenced by the free radical EPR signal. As shown in Fig. 6c, characteristic peaks of $^{\cdot}OH$ and $SO_4^{\cdot-}$ were displayed, affirming the formation of $^{\cdot}OH$ and $SO_4^{\cdot-}$ in the CoFe-MOF/PMS system. The emergence of EPR signals of $O_2^{\cdot-}$ (Fig. 6d) and $^1O_2$ (Fig. 6e) indicated the production of $O_2^{\cdot-}$ and $^1O_2$ radicals in the system. Consequently, the synergistic effect of $^{\cdot}OH$, $SO_4^{\cdot-}$, $O_2^{\cdot-}$, and $^1O_2$ free radicals achieved efficient degradation of pollutants (Fig. 6f).

Initially, Co^{2+} and Fe^{2+} activated the adsorbed HSO_5^- to produce $SO_4^{\cdot-}$ through eqn (9) and (10). Subsequently, $SO_4^{\cdot-}$ underwent reactions with H_2O or OH^- to generate $^{\cdot}OH$ (eqn (11)). The electrons of $HSO_5^{\cdot-}$ facilitated the reduction of Co^{3+} and Fe^{3+} to Co^{2+} and Fe^{2+} (eqn (12) and 13). HSO_5^- contributed to the production of $^1O_2$ by acquiring electrons (e^-) and forming SO_5^- (eqn(14)). Additionally, $SO_4^{\cdot-}$ and H_2O, generated during the oxidation of transition metals, were engaged in a reaction to produce OH (eqn (15)). The reaction between $SO_5^{\cdot-}$ and OH^- resulted in the generation of SO_4^{2-}, $^{\cdot}OH$, and O_2 (eqn (16)), wherein these three products actively participated in subsequent reactions. O_2 acquired electrons to yield $O_2^{\cdot-}$ (eqn (17)), and $O_2^{\cdot-}$ reacted with $^{\cdot}OH$ to generate $^1O_2$ (eqn (18)). Furthermore, on leveraging the reduction properties of TA, TA-M (III) acquired electrons to generate TA-M (II) (eqn (19)). In summation, the catalytic-cleaning mechanism of the CoFe-MOF/GO–TA/PMS system was ascribed to the synergistic effects of $^{\cdot}OH$, $SO_4^{\cdot-}$, $O_2^{\cdot-}$, and $^1O_2$ (eqn (20)). Derived from the preceding discoveries, Fig. 7f delineates the conceivable degradation mechanism of the CoFe-MOF/GO–TA/PMS system.

$$Co^{2+} + HSO_5^- \rightarrow Co^{3+} + SO_4^{\cdot-} + OH^- \quad (9)$$

$$Fe^{2+} + HSO_5^- \rightarrow Fe^{3+} + SO_4^{\cdot-} + OH^- \quad (10)$$

$$SO_4^{\cdot-} + H_2O/OH^- \rightarrow SO_4^{2-} + {}^{\cdot}OH \quad (11)$$

$$Co^{3+} + HSO_5^- \rightarrow Co^{2+} + SO_5^{\cdot-} + H^+ \quad (12)$$

$$Fe^{3+} + HSO_5^- \rightarrow Fe^{2+} + SO_5^{\cdot-} + H^+ \quad (13)$$

$$HSO_5^- + SO_5^- + e^- \rightarrow HSO_4^- + SO_4^{2-} + {}^1O_2 \quad (14)$$

$$SO_4^{\cdot-} + H_2O \rightarrow SO_4^{2-} + {}^{\cdot}OH + H^+ \quad (15)$$

$$2\,SO_5^{\cdot-} + 2\,OH^- \rightarrow 2\,SO_4^{2-} + 2\,{}^{\cdot}OH + O_2 \quad (16)$$

$$e^- + O_2 \rightarrow O_2^{\cdot-} \quad (17)$$

$$O_2^{\cdot-} + {}^{\cdot}OH \rightarrow {}^1O_2 + OH^- \quad (18)$$

$$TA\text{-}M(III) + e^- \leftrightarrow TA\text{-}M(II) \quad (19)$$

Table 4 Natural population analysis of charge distribution on RhB

Atom	f_k^0	Atom	f_k^0	Atom	f_k^0
C1	0.003	C12	−0.015	C23	−0.010
C2	0.019	C13	0.049	C24	0.007
C3	0.014	C14	0.001	C25	−0.024
C4	0.050	C15	−0.053	C26	−0.037
C5	0.014	C16	0.059	C27	0.007
O6	0.033	C17	0.031	C28	0.015
C7	−0.023	C18	0.041	C29	0.017
C8	0.123	C19	0.029	C30	0.008
C9	−0.121	C20	0.030	C31	0.029
C10	0.121	N21	0.010	O32	0.026
C11	0.021	N22	0.019	O33	0.047

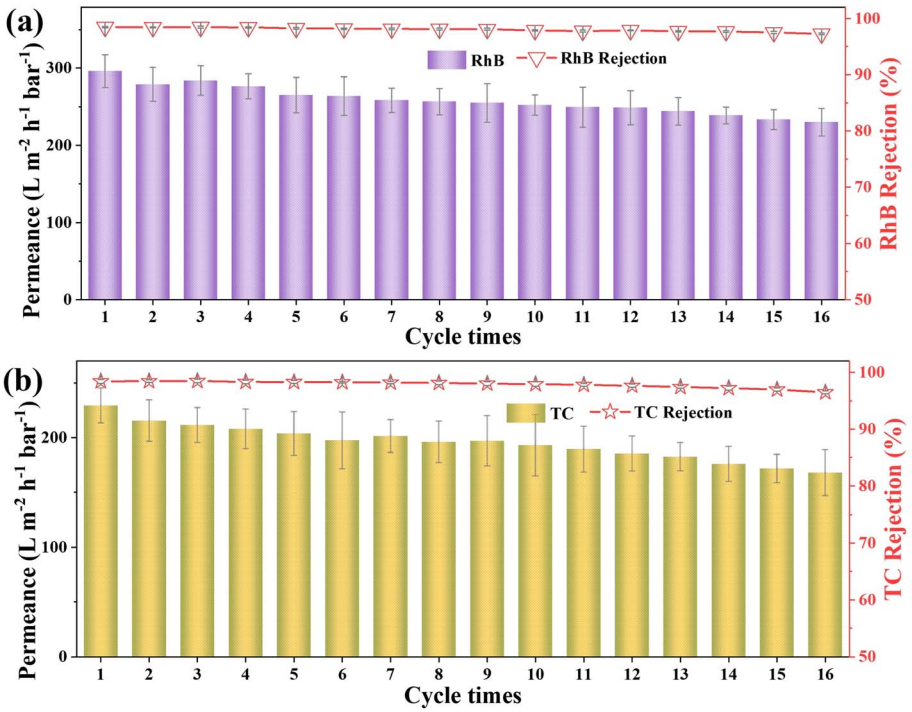

Fig. 8 Cycling separation performance of CoFe-MOF/GO–TA-10 for RhB (a) and TC (b). Conditions: [P] = 1.0 bar, [RhB] = 10 mg L^{-1}, [PMS] = 100 mg L^{-1}.

$$SO_4^{\bullet -} + {}^{\bullet}OH + O_2^{\bullet -} + {}^1O_2 + \text{Pollutants} \rightarrow \text{Degradation} \quad (20)$$

Theoretical calculations were conducted on the RhB structure (Fig. 7a) to identify vulnerable sites targeted by free radicals. The HOMO and LUMO denoted the highest/lowest energy occupied/unoccupied molecular orbitals. Examination of the HOMO of RhB revealed predominant contributions from O atoms (O32 and O33), C atoms (C3, C4, C8, C10, C15, C16, C17, C18, C19, C20, and C31), and N atoms (N22 and N23), forming the primary HOMOs where electrons could be readily extracted (Fig. 7b). Conversely, the LUMOs (Fig. 7c), where electrons would preferentially occupy, were chiefly influenced by N atoms (N22), C atoms (C10, C11, C12, C14, C16, C17, C18, C19, and C31), and O atoms (O6, O32, and O33). The Fukui function (f_k^0) provided a visual representation of RhB reactive sites for radical attacks.[37] Condensed Fukui functions, derived from Hirshfeld charges, were employed for a quantitative analysis of an atom potential as a reactive site (Table 4). Reactive sites exhibited a larger condensed Fukui function value compared to other regions. The most substantial f_k^0 was situated at C8 and C10, followed by C16, C15, C4, C13, O33, and C18, indicating favored reactive sites for radical attacks. By LC-MS analysis (Fig. S12†), the plausible degradation pathway of RhB could be inferred as shown in Fig. 7d. The labile amine group, influenced by free radicals and electrons (N21 and N22), underwent a reaction leading to the removal of $-C_2H_5$.[53] Subsequently, C10 experienced a free radical attack, resulting in bond cleavage and the formation of a molecule (M/Z = 269). Free radical impact on C8 induced ring-opening reactions, yielding a series of products (M/Z = 196 and 180).[54,55] Ultimately, the micro-molecules were degraded into H_2O and CO_2.

The cyclic catalytic-cleaning performance of CoFe-MOF/GO–TA-10 was scrutinized under a pressure of 1.0 bar utilizing RhB and TC solutions as pollutants. Fig. 8a shows that after 16 filtration cycles, the rejection and permeance of RhB gradually diminished, yet maintained high values of 97.26% and 230.11 L m^{-2} h^{-1} bar^{-1}, respectively. The reduction in RhB filtration performance was ascribed to the impairment inflicted upon the original intermolecular interaction and void structure of CoFe-MOF and GO–TA by PMS during the catalytic-cleaning process. As shown in Fig. S13,† throughout the experimental procedure, the leaching concentration of ions was consistently upheld below 0.27 mg L^{-1}, a level significantly below the threshold deemed environmentally toxic (5 mg L^{-1}). As showed in Fig. 8b, regarding the cycling performance of CoFe-MOF/GO–TA-10 on TC, the rejection and permeance of TC diminished to 96.48% and 167.74 L m^{-2} h^{-1} bar^{-1}, respectively, after 16 cycles. Overall, the cycling catalytic-cleaning performance of CoFe-MOF/GO–TA-10 was demonstrated to be excellent. This provided valuable insights into the stability and efficiency of the material in addressing pollutants such as dyes and antibiotics, opening avenues for further exploration and application in sustainable environmental remediation processes.

4 Conclusion

In this study, a pre-synthesized spindle-shaped CoFe-MOF was employed as the rigid framework. It was uniformly interspersed between a GO flexible bridge and TA cross-linking agent to

construct a high MOF proportion hybrid membrane, mimicking a "brick and mortar" structure. These distinctive layered membranes demonstrated exceptional separation performance for dyes and antibiotic. Specifically, the optimal CoFe-MOF/GO–TA-10 exhibited a noteworthy enhancement in the rejection of RhB, reaching 98.45%, coupled with a permeance of 296.17 L m^{-2} h^{-1} bar^{-1}. The cycling catalytic-cleaning performance of CoFe-MOF/GO–TA-10 was also considered excellent, with RhB permeance maintaining high values of 230.11 L m^{-2} h^{-1} bar^{-1}, even after 16 cycles, and the rejection was equally sustained at an elevated level of 97.26%. These findings underscore the exceptional catalytic-cleaning attributes of the MOF hybrid membrane. The catalytic-cleaning process through the CoFe-MOF/PMS system was discerned using quenching experiments, EPR tests, LC-MS analysis, and Gaussian calculations. The results indicated that CoFe-MOF/GO–TA-10 held promise for the treatment of water-soluble pollutants. Additionally, the substantial quantity of CoFe-MOF present proved advantageous for the catalytic-cleaning of the MOF hybrid membranes, characterized by a rigid-flexible mesh-like structure. Simultaneously, the GO flexible bridge expanded the permeance path of water molecules and heightened the adsorption separation of pollutants. The exceptional performance of membrane design enhanced the feasibility of rigid-flexible coupled MOF hybrid membranes in water treatment.

Data availability

The raw/processed data required to reproduce these findings cannot be shared at this time as the data also form part of an ongoing study.

Author contributions

Ruilong Zhang: investigation, validation, methodology, writing. Jun Zhao: writing – review & editing. Xiaohua Tian: investigation, writing – review. Jian Ye: investigation, conceptualization. Lulu Wang: investigation. Ifunanya Rejoice Akaniro: writing – review. Pan Jianming: investigation, resources, supervision. Dai Jiangdong: supervision, project administration.

Conflicts of interest

The authors declare that they have no known competing financial interests or personal relationships that could have appeared to influence the work reported in this paper.

Acknowledgements

This article was supported by the Jiangsu Funding Program for Excellent postdoctoral Talent (2023ZB453 and 2023ZB108), National Natural Science Foundation of China (22176218, 22008092, and 22378173), Postdoctoral Research Foundation of China (2022M721382), and Hong Kong Environment and Conservation Fund (2022-127).

References

1 S. Rojas and P. Horcajada, *Chem. Rev.*, 2020, **120**, 8378–8415.
2 F. Jia, L. Yang, L. Sun, D. Yu, Y. Song, Y. Wang, M. J. Kipper, J. Tang and L. Huang, *Water Res.*, 2023, **247**, 120693.
3 F. Jia, X. Xiao, A. Nashalian, S. Shen, L. Yang, Z. Han, H. Qu, T. Wang, Z. Ye, Z. Zhu, L. Huang, Y. Wang, J. Tang and J. Chen, *Nano Res.*, 2022, **15**, 6636–6654.
4 R. Zhang, Z. Zhou, Y. Wang, X. Dai, L. Chen and J. Dai, *J. Bionic Eng.*, 2021, **18**, 559–573.
5 J. Liu, R. Zhang, L. Wang, Y. Liu, X. Tian, X. Dai, J. Pan and J. Dai, *Sep. Purif. Technol.*, 2023, **319**, 124051.
6 J. Ye, J. Dai, D. Yang, C. Li, Y. Yan and Y. Wang, *Chem. Eng. J.*, 2021, **418**, 129383.
7 Z. Zhu, J. Ye, X. Tang, Z. Chen, J. Yang, P. Huo, Y. H. Ng and J. Crittenden, *Environ. Sci. Technol.*, 2023, **57**, 16131–16140.
8 Y. Wu, R. Lin, K. Zhang, J. Yan, F. Ma, J. Zhen and J. Pan, *Chem. Eng. J.*, 2023, **460**, 141891.
9 R. Zhang, J. Zhao, J. Ye, X. Tian, L. Wang, J. Pan and J. Dai, *J. Hazard. Mater.*, 2024, **468**, 133793.
10 K. Wang, Y. Li, L.-H. Xie, X. Li and J.-R. Li, *Chem. Soc. Rev.*, 2022, **51**, 6417–6441.
11 S. Xie, Z. Zhou, X. Zhang and J. Fransaer, *Chem. Soc. Rev.*, 2023, **52**, 4292–4312.
12 M. Zhu, Y. Liu, M. Chen, D. Gan, M. Wang, H. Zeng, M. Liao, J. Chen, W. Tu and W. Niu, *Chin. Chem. Lett.*, 2020, **31**, 2683–2688.
13 O. Shekhah, J. Liu, R. A. Fischer and C. Wöll, *Chem. Soc. Rev.*, 2011, **40**, 1081–1106.
14 K.-G. Liu, F. Bigdeli, A. Panjehpour, S. Hwa Jhung, H. A. J. Al Lawati and A. Morsali, *Coord. Chem. Rev.*, 2023, **496**, 215413.
15 A. Kirchon, L. Feng, H. F. Drake, E. A. Joseph and H.-C. Zhou, *Chem. Soc. Rev.*, 2018, **47**, 8611–8638.
16 Y. Liu, H. Chen, T. Li, Y. Ren, H. Wang, Z. Song, J. Li, Q. Zhao, J. Li and L. Li, *Angew. Chem., Int. Ed.*, 2023, **62**, e202309095.
17 H.-L. Hung, T. Iizuka, X. Deng, Q. Lyu, C.-H. Hsu, N. Oe, L.-C. Lin, N. Hosono and D.-Y. Kang, *Sep. Purif. Technol.*, 2023, **310**, 123115.
18 X. Shao, G. Yao, Z. Wang, Y. Chen, D. Yang, F. Qiu and T. Zhang, *J. Cleaner Prod.*, 2024, **434**, 139873.
19 H.-M. Ren, Y.-R. Liu, B.-Y. Liu, Z.-F. Li and G. Li, *Inorg. Chem.*, 2022, **61**, 9564–9579.
20 W.-H. Zhang, M.-J. Yin, Q. Zhao, C.-G. Jin, N. Wang, S. Ji, C. L. Ritt, M. Elimelech and Q.-F. An, *Nat. Nanotechnol.*, 2021, **16**, 337–343.
21 J. Ye, Y. Wang, Z. Li, D. Yang, C. Li, Y. Yan and J. Dai, *J. Hazard. Mater.*, 2021, **417**, 126028.
22 X. Zhao, W. Gao, W. Yao, Y. Jiang, Z. Xu and C. Gao, *ACS Nano*, 2017, **11**, 9663–9670.
23 Z. Liu, Z. Li, Z. Xu, Z. Xia, X. Hu, L. Kou, L. Peng, Y. Wei and C. Gao, *Chem. Mater.*, 2014, **26**, 6786–6795.
24 A. Xie, J. Cui, J. Yang, Y. Chen, J. Lang, C. Li, Y. Yan and J. Dai, *Appl. Catal., B*, 2020, **264**, 118548.
25 L.-H. Xu, Y. Li, S.-H. Li, M.-Y. Lv and Z.-P. Zhao, *J. Membr. Sci.*, 2022, **656**, 120605.

26 Y. Liu, M. Zhu, M. Chen, L. Ma, B. Yang, L. Li and W. Tu, *Chem. Eng. J.*, 2019, **359**, 47–57.
27 Y. Li, X. Zhang, A. Yang, C. Jiang, G. Zhang, J. Mao and Q. Meng, *J. Membr. Sci.*, 2021, **635**, 119521.
28 Z. Wang, J. Zhu, S. Xu, Y. Zhang and B. Van der Bruggen, *J. Membr. Sci.*, 2021, **633**, 119397.
29 S. Zhou, X. Feng, J. Zhu, Q. Song, G. Yang, Y. Zhang and B. Van der Bruggen, *J. Membr. Sci.*, 2021, **623**, 119058.
30 D. Liu, G. Pang, Z. Tang and S. Feng, *Inorg. Chem. Front.*, 2019, **6**, 2043–2049.
31 Y. Li, X. Yang, L. Yan, G. Dang, P. Sun, E. N. Nxumalo, B. B. Mamba and L. Shao, *J. Membr. Sci.*, 2024, **696**, 122526.
32 Y. Zheng, H. Bai, Z. Huang, X. Tian, F.-Q. Nie, Y. Zhao, J. Zhai and L. Jiang, *Nature*, 2010, **463**, 640–643.
33 H. Wan, J. Min, B. E. Carlson, J. Lin and C. Sun, *ACS Appl. Mater. Interfaces*, 2021, **13**, 13760–13770.
34 W. Ge, Z. Zhou, P. Zhang, Q. Zhang, Z. Cao, R. Zhang, Y. Yan and J. Dai, *J. Ind. Eng. Chem.*, 2018, **66**, 456–467.
35 M. J. Frisch, G. Trucks and H. B. Schlegel, *Gaussian 09W (Revision A.02)*, Gaussian Inc., Pittsburgh, PA, 2009.
36 A. E. Reed, L. A. Curtiss and F. Weinhold, *Chem. Rev.*, 1988, **88**, 899–926.
37 Y.-H. Zhou, S.-Y. Yang, M.-X. Wang, Y.-H. Guan and J. Ma, *Water Res.*, 2023, **243**, 120311.
38 J. Shi, B. Zhang, W. Wang, W. Zhang, P. Du, W. Liu, X. Xing, D. Ding, G. Lv, Q. Lv and L. Guo, *Chem. Eng. J.*, 2021, **426**, 131567.
39 A. Schneemann, V. Bon, I. Schwedler, I. Senkovska, S. Kaskel and R. A. Fischer, *Chem. Soc. Rev.*, 2014, **43**, 6062–6096.
40 G.-T. Vuong, M.-H. Pham and T.-O. Do, *Dalton Trans.*, 2013, **42**, 550–557.
41 X. Liu, H. Peng, J. Lu, Y. Ji, S. Li, J. Yuan, Q. Zhao and C. Gao, *Adv. Membr.*, 2023, **3**, 100059.
42 J. L. Fenton, D. W. Burke, D. Qian, M. Olvera de la Cruz and W. R. Dichtel, *J. Am. Chem. Soc.*, 2021, **143**, 1466–1473.
43 F. Yang, Y. Zhang, J. Huang, G. Gao, J. Zhu, J. Ma and L. Shao, *Sci. Bull.*, 2023, **68**, 29–33.
44 X. Sui, Z. Yuan, C. Liu, L. Wei, M. Xu, F. Liu, A. Montoya, K. Goh and Y. Chen, *J. Mater. Chem. A*, 2020, **8**, 9713–9725.
45 R. Mohamat, A. B. Suriani, A. Mohamed, M. Muqoyyanah, M. H. D. Othman, R. Rohani, M. H. Mamat, M. K. Ahmad, M. N. Azlan, M. A. Mohamed, M. D. Birowosuto and T. Soga, *Int. J. Environ. Res.*, 2021, **15**, 149–161.
46 H. Zeng, Z. Yu, L. Shao, X. Li, M. Zhu, Y. Liu, X. Feng and X. Zhu, *Chem. Eng. J.*, 2021, **403**, 126281.
47 R. Yue, T. Chen, Z. Ye, B. Barbeau and M. S. Rahaman, *J. Water Proc. Eng.*, 2021, **44**, 102443.
48 Y. Gao, S. Yan, Y. He, Y. Fan, L. Zhang, J. Ma, R. Hou, L. Chen and J. Chen, *J. Membr. Sci.*, 2021, **626**, 119192.
49 Y. Pan, Z. Shi, J. Li, Z. Zhang, X. Li, Z. Zhuang, Y. Mo, J. Liang, Z. Wang, M. An, Q. Luo and X. Chen, *J. Membr. Sci.*, 2023, **672**, 121465.
50 Y. Zong, Q. Long, L. Chen, A. Samadi, H. Luo, K. Liang, X. Wan, F. Liu, Y. Chen, Z. Zhang and S. Zhao, *J. Membr. Sci.*, 2024, **693**, 122328.
51 W. Tu, Y. Liu, M. Chen, L. Ma, L. Li and B. Yang, *Sep. Purif. Technol.*, 2022, **296**, 121398.
52 L. Wang, R. Zhang, X. Tian, J. Ye, J. Dai and J. Pan, *J. Membr. Sci.*, 2024, **695**, 122454.
53 D. Xu, X. Sun, X. Zhao, L. Huang, Y. Qian, X. Tao and Q. Guo, *Water, Air, Soil Pollut.*, 2018, **229**, 317.
54 H. Su, Y. Chu and B. Miao, *Environ. Sci. Pollut. Res.*, 2021, **28**, 33570–33582.
55 Y. He, S. Zhou, Y. Wang, G. Jiang and F. Jiao, *J. Mater. Sci.: Mater. Electron.*, 2021, **32**, 21880–21896.